Macromolecules

Article

Cite This: Macromolecules 2019, 52, 4739−4748

pubs.acs.org/Macromolecules

# Intramolecular and Intermolecular Packing in Polymer Crystallization

Shijun Wang,[†] Shichen Yuan,[†] Kun Wang,[†] Wei Chen,[‡] Koji Yamada,[§] Deborah Barkley,[∥] Tadanori Koga,[∥,⊥] You-lee Hong,[#] and Toshikazu Miyoshi*[,†]

[†]Department of Polymer Science, The University of Akron, Akron, Ohio 44325-3909, United States

[‡]National Synchrotron Radiation Lab, CAS Key Laboratory of Soft Matter Chemistry, Anhui Provincial Engineering Laboratory of Advanced Functional Polymer Film, University of Science and Technology of China, Hefei, P. R. China

[§]Advanced Processing Technology Unit, Research Center, Toyobo Co., Ltd. 2-1-1 Katata, Otsu, Shiga 520-0292, Japan

[∥]Department of Chemistry and [⊥]Department of Materials Science and Chemical Engineering, Stony Brook University, Stony Brook, New York 11794, United States

[#]RIKEN CLST-JEOL Collaboration Center, RIKEN, Yokohama, Kanagawa 230-0045, Japan

Supporting Information

**ABSTRACT:** Recently, the chain-folding structure of $^{13}$C-labeled poly(L-lactic acid) (PLLA) with different molecular weights ($M$) of 46K (small, $s$), 90K (middle, $m$), and 320K g/mol (large, $l$) in the solution-grown crystals [*Macromolecules* **2018**, *51*, 8729−8737] was studied by solid-state nuclear magnetic resonance (ssNMR). In this work, the chain-folding and packing structures, long period, and morphology of $^{13}$C-labeled $s$-, $m$-, and $l$-PLLA in the melt-grown crystals crystallized at $T_c$ = 90 and 150 °C are investigated by ssNMR, small-angle X-ray scattering (SAXS), wide-angle X-ray diffraction (WAXD), and polarized optical microscopy (POM), respectively. All the $s$-, $m$-, and $l$-PLLA adopt thermodynamically stable $\alpha$ crystals and large spherulites with a diameter of ∼2 mm at $T_c$ = 150 °C. A large supercooling induces kinetically favored disordered $\alpha'$ crystals and nodular structures for all three samples. By comparing the experimental $^{13}$C−$^{13}$C double quantum (DQ) buildup data with the simulated ones, we found that all three PLLA samples with different $M_w$s adopt adjacent re-entry structure with the same mean value of successive adjacent re-entry number, $n$, of 1.5−2 in both $\alpha$ and $\alpha'$ crystals under the assumption of full adjacent re-entry, $F$ = 100%. Through systematic studies on the chain-folding structure as functions of $T_c$ and $M_w$, it is concluded that the chain-folding process is a local event and is independent of the overall crystallization process. On the basis of the chain-folding and packing structures in both solution- and melt-grown crystals, contributions of the intramolecular and intermolecular packing to the order−disorder phenomenon of the overall packing structure will be discussed.

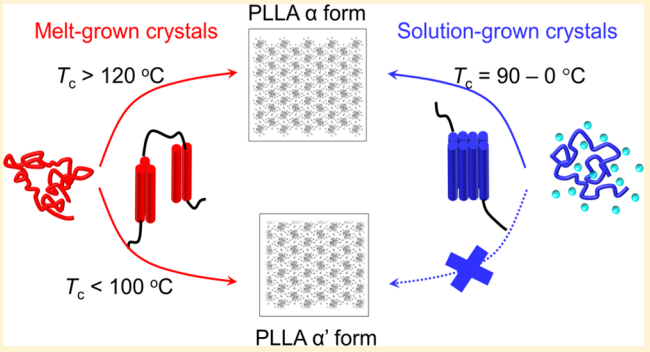


## 1. INTRODUCTION

Crystallization of long polymer chains induces structural formations at hierarchical length scales, i.e., conformation, packing, crystalline lamellae, and spherulites.[1−5] These structures and their time evolutions have been successfully characterized by various experimental techniques in the past decades.[6−10] One of the missing structures in polymer crystallization is the chain-level structure.[11,12] Because synthetic polymers consist of the same repeating monomer units, it is challenging to distinguish the intramolecular packing structure from the intermolecular one. So far, $^{2}$H or $^{13}$C isotope labeling combined with characterization techniques has been applied to study the chain-level structure of synthetic polymers (intramolecular structure) in the solution- and melt-grown crystals.[13−31] However, $^{2}$H/$^{1}$H polymer systems showed segregations under a low supercooling[13] and thus was limited to structural studies under a large supercooling.[14−19] To avoid this problem, Zheng et al. used monodisperse polyethylene (PE) oligomers only with the chain end labeled by $^{2}$H and studied the chain-level structure of PE during isothermal crystallization by in-situ neutron scattering.[20] Recently, our group developed a novel experimental strategy to access the detailed chain-folding structures in the melt- and solution-grown crystals[21−31] by using selective $^{13}$C isotope labeling and $^{13}$C−$^{13}$C double quantum (DQ)[32] NMR spectroscopy. The $^{13}$C−$^{13}$C DQ NMR provides a measure of apparent dipolar coupling strengths for a given $^{13}$C site, which represent the root-mean-square sum of many $^{13}$C−$^{13}$C pair couplings which are determined by chain

**Received:** April 6, 2019
**Revised:** May 25, 2019
**Published:** June 10, 2019






DOI: 10.1021/acs.macromol.9b00702
*Macromolecules* 2019, 52, 4739−4748

trajectory of $^{13}$C-labeled polymers.[21−31] The dipolar coupling strength is inversely proportional to third power of the internuclear distance. Thereby, this method is particularly sensitive to a short-range structure (<∼7 Å).[32] A very tiny isotope effect of $^{13}$C/$^{12}$C and a lower labeling ratio of $^{13}$C led to cocrystallization of $^{13}$C/$^{12}$C polymer chains even under a very small supercooling.[21−23,25,26] Thus, this technique has been successfully applied to study the local intrachain structure of several synthetic polymers in both solution- and melt-grown crystals.[21−31]

In solution crystallization, crystal morphology drastically changes from facet single crystals to circular or dendrite crystals as a function of kinetics.[22,25,27,28,33−40] It has been debated as to whether or not the morphological change of the solution-grown crystals is related to the chain-level structures.[14,33−36,39,41−44] Hong et al. demonstrated that (i) the local chain-folding structure of *isotactic* poly(butene-1) (*i*PB1) adopts the adjacent re-entry rich cluster in the hexagonal single crystals and circular crystals and (ii) its mean size is independent of morphologies formed at different crystallization temperatures ($T_c$s).[22,24,25] Similarly, Wang et al. reported that PLLA chains with different $M_w$s of 46K−326K g/mol adopt the same cluster sizes formed via adjacent re-entry structure in both facet single crystals and dendrites.[27,28] It was suggested that the formation of the nanoclusters is triggered in terms of worse solvent−polymer interaction and not affected by experimentally available kinetics while the aggregation of the nanoclusters is affected by kinetics and consequently leads to morphological differences as a function of $T_c$. Such a crystallization mechanism is well consistent with the bundle[41,42] and aggregation models[43,44] but contradicts with the Lauritzen−Hoffman (LH) model,[46] where the crystallization regime is divided into I, II, and III from high to low $T_c$s.

In the condensed melts, entanglements of polymer chains significantly affect viscosity[47] as well as crystallization kinetics.[46] In rheological aspects, it is known that individual polymer chains have a critical segment length which can reflect the entanglement extent, called as a critical molecular weight, $M_c$.[47] In a relatively low molecular weight sample $M < M_c$, the viscosity, $\eta$, of polymer in the melt state is simply proportional to $M$ ($\eta \propto M$).[47] A very high mobility of polymers without entanglements leads to only regime I.[42] By use of small-angle X-ray scattering (SAXS) and the longitudinal acoustic mode (LAM) of Raman spectroscopy, it was indicated that polyethylene (PE) (weight-average-molecular weight, $M_w$ = 2000−5500)[42,48−50] and poly(ethylene oxide) (PEO) ($M_w$ = 1000−5000)[51,52] adopt the successive adjacent re-entry folds with folding number, $n$, of 0−3. According to these facts, it is understood that the chain-folding process is essential even in the highly condensed melt crystallization. Above $M_c$, $\eta \propto M^{3.4}$ is established in PE,[47] and a highly entangled network leads to slow kinetics of polymer crystallization.[46] Crystallization kinetics of high-$M$ polymers including PE,[46] *i*PB1,[53] PLLA,[54−57] and so on can be described in terms of regimes II and III even in a wide $T_c$ range. These facts imply that the crystal growth kinetics is highly related to the presence and absence of entanglements of the polymer chains.

Recently, Hong et al.[25] reported that *i*PB1 with $M_w$ = 37K g/mol adopts the $n$ values of 1.7−2 at $T_c$s of 95 and ∼0 °C (quenched into icy water) well above and below regime II−III transition temperatures of 77−82 °C.[53] Recent molecular dynamics (MD) simulation studies on the coarse-grained poly(vinyl alcohol) (PVA) model[58−61] and Monte Carlo (MC) simulations on PE also indicated limited $n$ values due to entanglements.[62] If $M_e$ or $M_c$ is a crucial factor to determine $n$ of long polymer chains in the melt-grown crystals, understanding $M$ and kinetics effects on the chain-folding structure is definitively necessary. To the best of our knowledge, there are no successful studies on the chain-folding structure of long polymer chains in the melt-grown crystals as functions of both $M$ and kinetics.[18]

In this study, we have two aims. The first aim is to understand the $M$ and kinetics effects on the chain-folding structure of a semicrystalline polymer in the melt-grown crystals. $^{13}$C $CH_3$-labeled PLLA samples with different $M_w$s of 46K, 90K, and 326K g/mol,[27,28] which are well above a reported mean value of entanglement molecular weight, $M_e$, of PLLA in the melt state (3.2K g/mol),[63] are used in this work. Moreover, two $T_c$s of 150 and 90 °C well above and below the reported regime II−III transition of 115−120 °C[54−57] are chosen to study the kinetics effects on the chain-level structures. The high $T_c$ chosen in the experiment is slightly higher than a reported regime I−II transition temperature of 147 °C.[56] It will be revealed how the crystallization kinetics and $M$ affect the chain-folding structure of PLLA in the melt-grown crystals. The second aim is to understand how the intramolecular and intermolecular packing structures contribute to the overall packing structure in the solution- and melt-grown crystals. Wang et al. reported that PLLA solution-grown crystals adopt only thermodynamically stable $\alpha$ crystals under a wide $T_c$ range of ∼0−90 °C.[27,28] On the other hand, high and low $T_c$s of >120 °C and <100 °C induce thermodynamically stable $\alpha$ and kinetically favored $\alpha'$ crystals in the melt-grown crystals, respectively.[64−67] *Why do the solution-grown crystals prefer thermodynamically stable α crystals even under a rapid quenching? Why does the order−disorder (α−α′) transition occur in the melt-grown crystals as a function of $T_c$?* To the best of our knowledge, there is no discussion about kinetics effects on different packing selections between the solution and melt-grown crystals. The chain-folding structure of PLLA in the melt- and solution-grown crystals provides a mean size of the intramolecular packing cluster. We will discuss the contributions of both intramolecular and intermolecular packing to order and disorder phenomena in the melt-grown crystals.

## 2. RESULTS AND DISCUSSION

**2.1. Morphology and Packing Structure of the PLLA Melt-Grown Crystals.** Figures 1a and 1b show polarized optical microscope (POM) images for the *m*-PLLA sample crystallized at $T_c$ = 150 and 90 °C, respectively. The images clearly indicate largely different nucleation densities and morphologies at different $T_c$s. At $T_c$ = 150 °C, the nucleation sites were really limited, and the low nucleation density led to the growth of each spherulite with a diameter larger than ∼2 mm. On the other hand, the nucleation density was extremely high, and thus the growth process was limited at $T_c$ = 90 °C, where the primary nucleation dominantly result in nodular morphology. The observed morphologies are well consistent with the previous reports on the melt-grown crystals.[7,56,65]

Figures 1c and d show the wide-angle X-ray diffraction (WAXD) profiles for the *m*-PLLA sample at $T_c$ = 150 and 90 °C, respectively. The former shows two main peaks corresponding to ⟨110⟩ and ⟨200⟩ at $2\theta$ = 16.7° and 19.1°, respectively, with other several satellite peaks, which indicate the thermodynamically stable $\alpha$ crystals with $a$ = 10.66, $b$ = 6.16, and $c$ = 28.88 Å at 25 °C.[68] The PLLA stems in the $\alpha$ crystals adopt left-handed $10_7$ helices possessing five discrete sites with different torsion angles



DOI: 10.1021/acs.macromol.9b00702
Macromolecules 2019, 52, 4739−4748

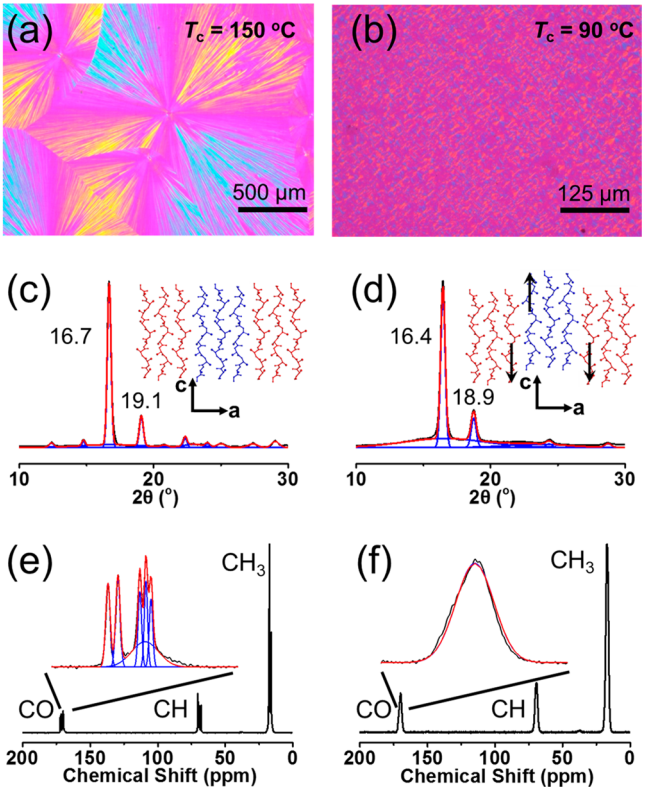


**Figure 1.** POM images with a sensitive color plate for *m*-PLLA melt-grown crystals at (a) $T_c$ = 150 and (b) 90 °C. The WAXD profiles (black lines) and the simulated peaks (blue and red lines) for the PLLA melt-grown crystals at (c) $T_c$ = 150 and (d) 90 °C. The $^{13}$C CPMAS spectra for the PLLA melt-grown crystals at (e) $T_c$ = 150 and (f) 90 °C for the blended PLLA of the labeled PLLA and nonlabeled PLLA with a ratio of 1:9. The inserted figures are for the enlarged CO peaks and the simulated peaks.

($\varphi$, $\psi$, $\omega$) in the backbone with A (−68.2°, 151.6°, 175.4°), B (−63.0°, 154.5°, 165.0°), C (−65.8°, 158.7°, 178.1°), D (−66.0°, 163.9°, 167.3°), and E (−58.0°, 150.0°, 168.6°).[68] A similar diffraction pattern was observed for *m*-PLLA crystallized at $T_c$ = 90 °C. Two main peaks appear at 16.4° and 18.7°, which are characteristic peaks for the $\alpha'$ crystals with $a$ = 10.80, $b$ = 6.20, and $c$ = 28.80 Å.[69] The unit size is slightly larger (0.6 and 1% along $a$ and $b$ axes, respectively) than that for the $\alpha$ crystals. Recently, Tashiro et al. carefully analyzed the diffraction pattern of the $\alpha'$ form and suggested that (i) the local torsion angles in the helical conformation of $\alpha'$ as ($\varphi$, $\psi$, $\omega$) = (−55° to 81°, 175° to −160°, 183° to −152°) are slightly different from those in the $\alpha$ crystal, (ii) the crystal domain of the $\alpha'$ form is smaller than that of the $\alpha$ form, and (iii) there is height disorders along the $c$ axis at the boundary of two connective domains in the $\alpha'$ crystals as schematically illustrated in Figures 1c and 1d.[69] Additional possible structural disorders in the $\alpha'$ crystals are up- and downward orientations of individual helices.

Applying Gaussian peaks (blue lines in Figures 1c and 1d) to the WAXD profiles determined the crystallinity ($\Phi$) to be 75 and 50% for the $\alpha$ and $\alpha'$ crystals, respectively. The WAXD patterns of *s*- and *l*-PLLA are also shown in Figure S1, and all the crystallinity is listed in Table 1. Figure 1e,f depicts $^{13}$C CPMAS NMR spectra for $^{13}$C 30% $CH_3$-labeled *m*-PLLA blended with nonlabeled PLLA with a blending ratio of 1:9. The $CH_3$ signal at $T_c$ = 150 °C shows doublet peaks with an intensity ratio of 4:1 at 17.1 and 16.4 ppm, respectively, which are typical line shapes for

**Table 1. Crystallinity ($\Phi$), Long Spacing ($l_0$), and the Average Chain-Folding Number ($n$) for the Crystals as Functions of $T_c$ and $M_w$**

| | $T_c$ (°C) | $\Phi^a$ (%) | $l_0$ (nm) | $n$ |
|---|---|---|---|---|
| *s*-PLLA | 150 | 75 | 28.7 | 1.5−2 |
| | 90 | 50 | 23.7 | |
| *m*-PLLA | 150 | 75 | | 1.5−2 |
| | 90 | 53 | | |
| *l*-PLLA | 150 | 68 | 28.7 | 1.5−2 |
| | 90 | 47 | 23.7 | |

[a]Determined by peak fitting of WAXD profiles.

the $\alpha$ crystals.[27,28,66,70−72] The CH and CO groups show multiple splitting peaks in the $\alpha$ crystals; e.g., the expanded CO signal shows five sharp peaks corresponding to five sites of A−E in the crystalline region.[27,28] Applying five Gaussian peaks plus one broad peak to the amorphous CO line shape could determine the crystallinity as 70%, which is slightly smaller than the WAXD result. The crystallinity for the $\alpha$ crystals for *s*- and *l*-PLLA was also determined to be 75 and 68%, respectively. Note that $\Phi$ = 75−68% for *s*-, *m*-, and *l*-PLLA the melt-grown crystals at $T_c$ = 150 °C is larger than $\Phi$ = 58−60% for the same samples in the solution-grown single crystals at $T_c$ = 90 °C.[27,28]

The $\alpha'$-rich sample at $T_c$ = 90 °C exhibited only one broad line shape for all three peaks. The spectral pattern and chemical shift values for the $\alpha'$-rich sample are very similar to those for the quenched glasses as depicted in Figure S2 and in the reported literature.[66,72] Hsu et al.[73,74] reported that more than 80% of the chains adopt similar helical conformations with $10_7$ helices in the $\alpha$ crystals by using Raman spectroscopy. The results suggest that the local conformations in the PLLA glasses are very similar to those in the $\alpha$ crystals. Currently, we are investigating the local conformations of $^{13}$C CH doubly enriched PLLA glasses by using ssNMR spectroscopy. The result will be reported elsewhere in the future. On the other hand, the XRD results indicate that both $\alpha$ and $\alpha'$ crystals adopt three-dimensional long-range order[68,69] while only the glasses do not possess such order. The structural differences might arise from characteristic length scales of different characterization techniques: XRD is sensitive to the structure with a three-dimensional long-range order while Raman and NMR are sensitive to the local structure.

Small-angle X-ray scattering (SAXS) provides that the long period ($l_0$) of *l*- and *s*-PLLA crystals at $T_c$ = 150 and 90 °C was 28.7 and 23.7 nm, respectively (see Figure S3). The $l_0$ values were well consistent with the previous reports.[54] Based on the crystallinity of both samples and similar densities for the glasses (1.25 g/cm$^3$)[75] and $\alpha$ crystals (1.26 g/cm$^3$),[68] the crystal layer thickness, $l$, was determined to be 21.5 and 11.9 nm at $T_c$ = 150 and 90 °C, respectively. Usually, the long period of semicrystalline polymers is inversely proportional to $T_m - T_c$. Kawai et al. for the first time reported the unique $l_0$ value of PLLA at $T_c$ = 90 °C, which was larger than the calculated value from the linear relationship of $l_0 \propto 1/(T_m - T_c)$.[54] Such uniqueness was explained in terms of the high mobility of the chain dynamics in the $\alpha'$ phase by Chen et al. using ssNMR spectroscopy.[71,72] Alternatively, Lotz found a transient metastable $\beta$ phase prior to the $\alpha'$ phase and also considered the role of chain mobility in the metastable form.[76]

For all the PLLA samples, both $\Phi$ and $l_0$ were independent of $M_w$ at the same $T_c$. With decreasing $T_c$, The $\Phi$ value is lowered to about 50% for all three samples at $T_c$ = 90 °C, which are



DOI: 10.1021/acs.macromol.9b00702
Macromolecules 2019, 52, 4739−4748

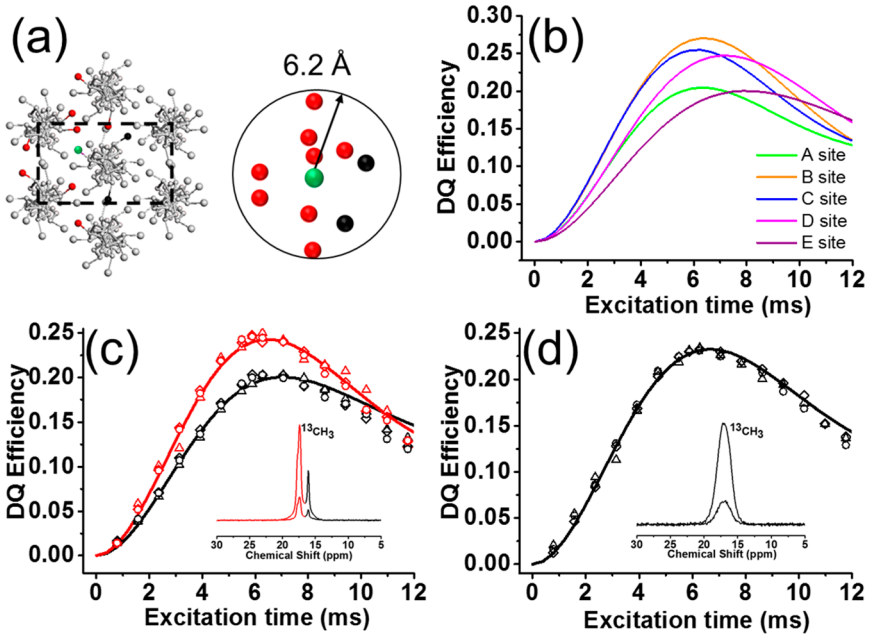


**Figure 2.** (a) Packing structure of the PLLA $\alpha$ form crystal with an orthorhombic crystal unit cell with $a$ = 10.66, $b$ = 6.16, and $c$ = 28.88 Å.[68] The 11 spin system including eight interstem interacted spins and two intrastem interacted spins surrounding the reference D spin (green color) within a distance of 6.2 Å was schemed as an example. The other four sites spin environments can be referred to ref 27. (b) Simulated DQ buildup curves at the five conformational sites (defined as A−E sites in ref 27) with $T_2$ of 9.5 ms. (c) Experimental DQ data of PLLA $\alpha$ crystals for *s*- (circles), *m*- (triangles), and *l*-PLLA (lozenges) at two peaks of 17.4 ppm (red ones) and 16.1 ppm (black ones) in (c), respectively. The red and black simulated curves were based on the atomic coordinates of $CH_3$ carbons and $T_2$ of 9.5 ms. (d) Experimental DQ data of PLLA $\alpha'$ crystals for *s*- (circles), *m*- (triangles), and *l*-PLLA (lozenges). The $^{13}C$ CPMAS SQ (top) and DQ (bottom) NMR spectra for $^{13}C$ 30% $CH_3$-labeled *m*-PLLA crystals crystallized at $T_c$ = 150 and 90 °C are shown in the inserted figures in (c) and (d). The DQ excitation time was 6.27 ms.

attributed to slowing down of the chain mobility of PLLA in the melt state as well as $\alpha'$ crystals ($T_g$ of ∼60 °C).

Figure 2a shows five $10_7$ helical stems with four corners and one center in the unit cell of the $\alpha$ crystals in the *ab* plane. According to the conformation of $10_7$ helix determined by XRD, the chains adopt discrete five conformations in $10_7$ helix in the $\alpha$ crystals. The $^{13}C-^{13}C$ spin pairs in the multiple spins system of the $^{13}C$ 30% $CH_3$-labeled PLLA chains are excited by DQ NMR spectroscopy. The dipolar interaction of the spin pairs is proportional to the reciprocal of third power of their internuclear distance,[32,77] and thus the short $^{13}CH_3-^{13}CH_3$ internuclear distances <7 Å were used in numerical spin-dynamics simulations.[78]

The $^{13}C$ CP MAS spectra of single quantum (SQ, top) and DQ (bottom) for the $^{13}C$ 30% $CH_3$-labeled *m*-PLLA melt-grown crystals at $T_c$ = 150 and 90 °C are illustrated in Figure 2c,d. The PLLA crystals at 150 °C showed two $CH_3$ peaks at 17.4 and 16.1 ppm, with an intensity ratio of 4:1, respectively. The experimental DQ data for *m*-PLLA (triangle) corresponding to the peaks at 17.4 ppm (red) and 16.1 ppm (black) are plotted in Figure 2c. The maximum DQ efficiency ($\xi_{max}$) was defined as the intensity ratio of the DQ signal to the SQ one of the methyl groups. The $\xi_{max}$ values at 17.4 and 16.1 ppm were 0.25 at $t_{ex}$ = 6.27 ms and 0.20 at $t_{ex}$ = 7.06 ms, respectively. These results indicate that spin environments at the five sites are heterogeneous in the $\alpha$ crystals. The same result was also obtained in the solution-grown crystals.[27,28]

In the simulation, the 11−12 spin systems including a reference spin at five sites of A−E were used (see details in ref 27). For example, one spin system including the D site as a reference spin colored by green and maximum ten neighbor spins within 7 Å is schematically illustrated in Figure 2a. The DQ buildup curves for all two spin pairs between a reference spin and each of the interacted spins were numerically simulated by using SPINEVOUTION,[78] where the atomic coordinates of the $CH_3$ carbons in the $\alpha$ crystals determined by XRD were used.[64] At each site among five sites, 2036 or more DQ buildup curves were simulated and averaged by weighting individual curves statistically to obtain the average curve.[27,28] The DQ simulated curves at the A−E sites are depicted in Figure 2b (see details in ref 27). Different DQ curves at the A−E sites indicate heterogeneous conformations and packing structures in the $\alpha$ crystals. The experimental DQ curve for the main signal at 17.1 ppm was reproduced by averaging four fast buildup curves among the five (red curve in Figure 2c). The DQ curve for the minor peak at 16.4 ppm could not be reproduced by using the slowest curve among the five but was well fitted by using averaging the slowest and the second slowest curves (black curve in Figure 2c), respectively, under the assumption of $T_2$ = 9.5 ms. These simulated curves could reproduce the experimental data for the *m*-PLLA $\alpha$ melt-grown crystals at $T_c$ = 150 °C as depicted in Figure 2c. The experimental DQ curves for $^{13}C$-labeled *s*- (circle) and *l*-PLLA (lozenge) $\alpha$ crystals at $T_c$ = 150 °C are also plotted in Figure 2c and are well consistent with the experimental *m*-PLLA curve. By comparisons of the experimental and simulated DQ buildup curves, it was demonstrated that the three PLLA samples possess the same $CH_3-CH_3$ internuclear distances with each other. From the $CH_3-CH_3$ distances, the mean value of chain center to center distance, $R$ can be extracted to 6.2 Å, which is well consistent with that determined by XRD (6.22 Å).[68]

As described above, the $^{13}C$-labeled *m*-PLLA $\alpha'$ crystals formed at 90 °C show only one broad peak at 16.8 ppm in Figure 2d. The mean conformation in the $\alpha'$ crystals are similar to that


DOI: 10.1021/acs.macromol.9b00702
*Macromolecules* 2019, 52, 4739−4748

in the $\alpha$ crystal. The DQ experimental data for $^{13}$C-labeled *m*-PLLA $\alpha'$ crystals (triangle) is shown in Figure 2d, and the $\xi_{max}$ value was ca. 0.23 at $t_{ex}$ = 6.27 ms. To the best of our knowledge, atomic coordinates of the $CH_3$ carbon in the $\alpha'$ crystals are not reported.[71] Therefore, we could not simulate the DQ curves for the $\alpha'$ crystals. However, the unit cell density and the helical pitches of the $\alpha'$ crystals are very similar to those in the $\alpha$ crystals.[68,69] Therefore, the atomic coordinates for the simulation parameters of the $\alpha$ crystals were used to reproduce the local packing structure for the $\alpha'$ crystals. The experimental data could be replicated by averaging of the DQ curves for all five sites in the $\alpha$ crystals (Figure 2d). Note that the analysis does not exclude contributions of the amorphous signal to the apparent DQ buildup curve for the $\alpha'$-rich samples because any relaxation filter cannot remove out the amorphous components due to the frozen molecular dynamics in the amorphous region at 25 °C. Therefore, it is interesting for us to understand how the amorphous and crystalline regions contribute to the apparent DQ curves.

To investigate the local packing structure of the amorphous regions of the $\alpha'$-rich sample, PLLA glasses were prepared by rapid quenching PLLA from 200 °C into the icy water at 0 °C. The $^{13}$C CPMAS NMR spectrum and XRD confirmed a glassy structure (Figures S2 and S4). Under the assumption of PLLA glasses adopting $10_7$ helices, the packing information can be investigated by the $^{13}$C−$^{13}$C DQ buildup curve. Figure 3

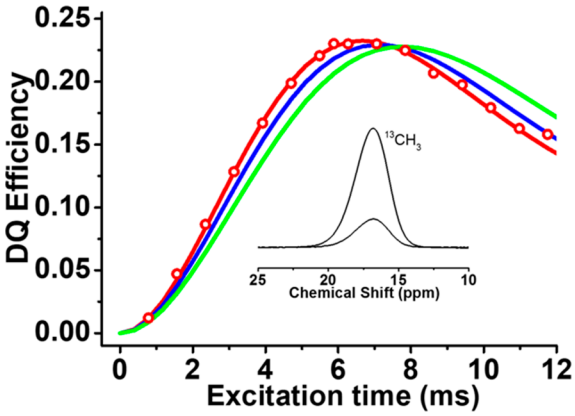


**Figure 3.** Experimental DQ buildup curve for $^{13}$C 30% $CH_3$-labeled *m*-PLLA glasses (red open circles) and simulated curves under the assumptions of $10_7$ helical conformations and *R* of 6.2 (red), 6.3 (blue), and 6.5 Å (green) The $^{13}$C CPMAS SQ (top) and DQ (bottom) NMR spectra for $^{13}$C 30% $CH_3$-labeled *m*-PLLA glasses are inserted.

represents the DQ curve of $^{13}$C 30% labeled PLLA glasses (red open circles) with $\xi_{max}$ of 0.23 at $t_{ex}$ = 6.27 ms. The experimental curve is very close to that for the $\alpha'$-rich samples. Thereby, we simply assumed that the glassy structures have very similar packing structure and conformation with those in the $\alpha'$ ($\alpha$) crystals. The simulated red, blue, and green curves correspond to the $\alpha$ packing structure with the *R* value of 6.2, 6.3, and 6.5 Å, respectively. Comparisons of the simulated and experimental curves suggest that the $\langle R \rangle$ value is 6.2 Å in the glasses, which is consistent with that for the $\alpha'$ ($\alpha$) crystals This result is supported by the facts that (i) the density of the PLLA glasses (1.25 g/cm$^3$)[75] is very close to that of the $\alpha$ (1.26 g/cm$^3$)[68] and (ii) the glasses adopt similar helical conformations with that in the $\alpha$ crystals.[73,74]

**2.2. Chain-Folding Analysis on the Melt-Grown Crystals.** In the unit cell of the $\alpha$ crystals, the left-handed stem located at the four corners and the center adopts upward and downward orientations, respectively. Considering configurationally constraints on the left-handed helices, the chain folding occurs only between the antiparallel ones. Such constraints limit folding pathways in the chiral polymer crystals. For example, several possible folding models are schematically depicted in Figure 4a. Here, the adjacent re-entry structure from the left corner in the unit cell was generated. One model is along ⟨110⟩. One spin system with a reference D spin colored by green in the center stem in the unit cell (Figure 4a) is used to explain impacts of the chain-folding structure to the DQ buildup curves. As mentioned above, this reference spin interacts with ten neighbor spins in $^{13}$C-labeled PLLA. In the case of the blend samples, the chain trajectory of a single $^{13}$C-labeled chain generates five interacted spins as illustrated in Figure 4a.[27,28] The reduced spin number lowers down the DQ buildup curve. The simulated DQ curves based on the folding path along ⟨110⟩ are plotted as a function of *n* in Figure 4b. With increasing the *n* value, the height of the DQ curves significantly increases due to reducing chain-end effect. The other two zigzag models are schematically illustrated in Figure 4a. The effective folding directions are along ⟨100⟩ (middle in Figure 4a) and ⟨010⟩. Similarly, one spin system using the same reference spin of D in the ⟨010⟩ and ⟨100⟩ models was considered. In the former, the neighbor spin number is six, which is the same with that in the linear ⟨110⟩ model and is lower than eight in the latter. The different chain trajectories generate different spin densities and topology, which result in the different buildup curves. Among the three models, the ⟨100⟩ zigzag model generates the highest DQ buildup curve as depicted in Figure 4c.

In the experiments, $^{13}$C-labeled chains were diluted by nonlabeled ones with a blending ratio of 1:9, and the blend samples were cocrystallized at $T_c$ = 150 and 90 °C. The experimental DQ buildup curves for the *s*-, *m*-, and *l*-PLLA blends melt-grown crystals at $T_c$ = 150 °C are plotted in Figure 5a−c, where only the DQ curves for the main peak at 17.4 ppm are shown. $\xi_{max}$ = 0.125 for the $^{13}$C-labeled *l*-PLLA blends is much lower than that of the $^{13}$C-labeled ones ($\xi_{max}$ = 0.25). This is a direct evidence for cocrystallization of $^{13}$C-labeled chains with abundant nonlabeled chains at the stem levels. The best-fit simulated curve to the experimental data gave the *n* values of the PLLA samples under the assumption of *F* = 100%. In the single row ⟨110⟩ model, the simulated curve with *n* = 2 (red line) could reproduce the experimental data (Figure 5a). The ⟨100⟩ zigzag structure could reproduce the experimental data under the assumption of *n* = 1.5 (black curve) where 1.5 means *n* = 1 and 2 with equal fractions (Figure 5a). Because of the similarity of the DQ curves, current results could not specify one of three models. All three models might be included in the real case of crystallization. In the $^{13}$C-labeled *m*- and *l*-PLLA melt-grown blend samples at $T_c$ = 150 °C, the same $\xi_{max}$ of 0.125 was obtained as shown in Figures 5b and 5c, respectively. The fitting curve used in Figure 5a could well reproduce the experimental curves in Figure 5b,c. This means that $M_w$ does not affect the successive adjacent re-entry number at the high $T_c$ well above the regime II−III transition temperature of 115−120 °C.[54−56]

At $T_c$ = 90 °C, the experimental DQ curves for all the three samples in the $\alpha'$ crystals (Figure 5e−g) were well consistent with each other. More surprisingly, these curves were very close to those in the $\alpha$ crystals. The simulated DQ curves based on the ⟨100⟩ zigzag model with *n* = 1.5 and linear ⟨110⟩ with *n* = 2,


DOI: 10.1021/acs.macromol.9b00702
*Macromolecules* 2019, 52, 4739−4748

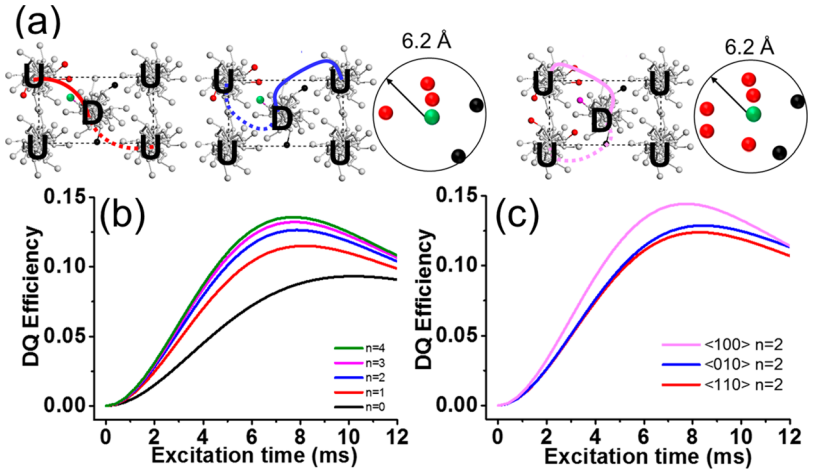


**Figure 4.** (a) Different chain-folding models including a linear chain-folding along ⟨110⟩ (left) and zigzag along ⟨010⟩ (middle) and ⟨100⟩ (right) and corresponding interacted spin systems at the reference D spin colored by green.[27,28] (b) DQ curves for the $^{13}$C-labeled PLLA melt-grown blend crystals with nonlabeled chains with a blending ratio of 1:9 as a function of $n$ along the ⟨110⟩ plane. (c) Simulated DQ curves in the three models with $n$ = 2.

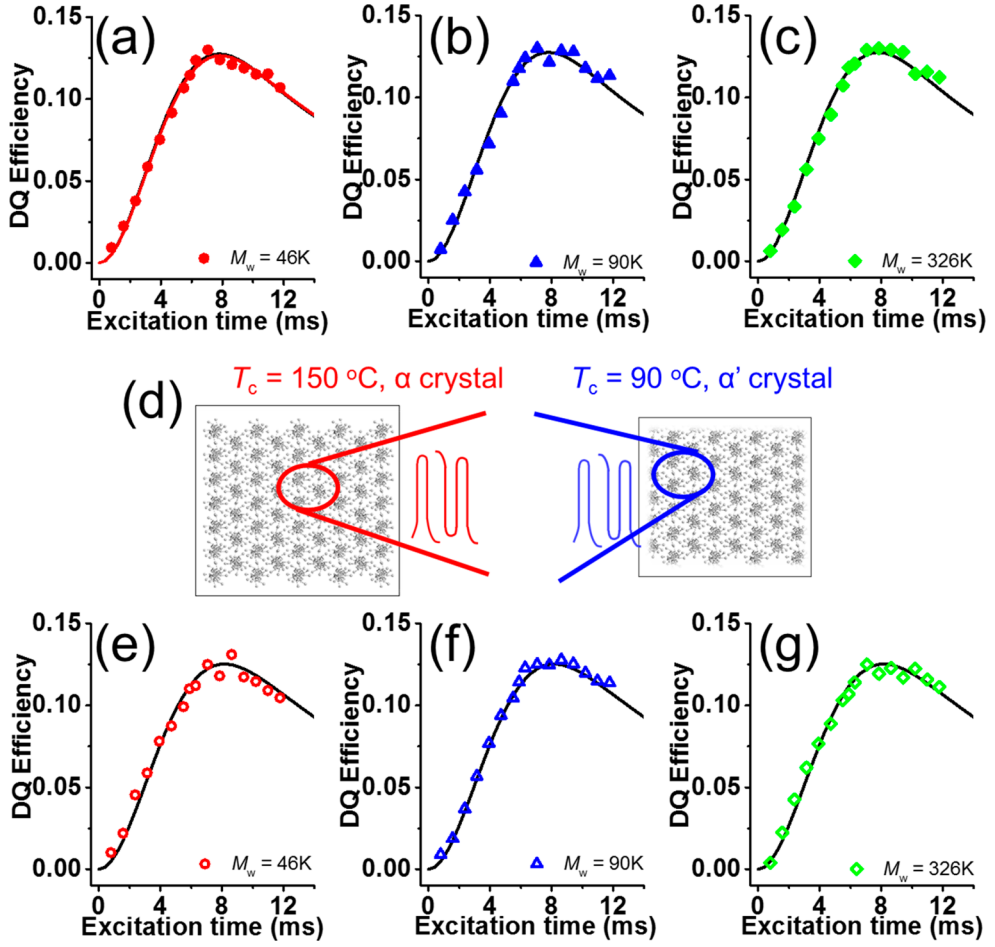


**Figure 5.** DQ experimental buildup curves for $^{13}$C 30% $CH_3$-labeled PLLA in the melt-grown blend crystals with nonlabeled PLLA with $M_w$ = 46K (a, e), 90K (b, f), and 320K g/mol (c, g) at $T_c$ = 150 °C (a–c) and 90 °C (e–g). The solid lines represent the simulation curves based on $n$ = 2 for linear model along the ⟨110⟩ plane. (d) Schematic illustrations for chain-packing domains for the PLLA crystals based on the XRD results in Figure 1c,d and the chain-folding structures at 150 and 90 °C (d).

which were used in the folding analysis for the $\alpha$ crystals, could reproduce all the three experimental curves at $T_c$ = 90 °C. Only the simulated curve based on the ⟨100⟩ model with $n$ = 2 is illustrated in Figure 5e–g. These experimental results prove that the chain-folding structures are independent of both $M_w$ and the experimentally used kinetics even well above and below regime II–III transitions.[54−56] Moreover, the local chain-folding structure is not a source to induce the $\alpha$ and $\alpha'$ crystals (see more details in the Discussion section). The folding number of the PLLA melt-grown crystals determined in this study is much



DOI: 10.1021/acs.macromol.9b00702
*Macromolecules* 2019, 52, 4739−4748

smaller than that of the same PLLA samples in the solution-grown crystals ($n$ = 7 in double row)[27,28] and is very similar to that of *i*PB1 melt-grown crystals ($n$ = 1.7−2.0)[25] and $n \sim 1.2$ predicted by the PVA coarse-grained model by Sommer and Luo.[58,59] In the early days, Hoffman proposed variable cluster models for PE melt-grown crystals in regime III,[79] where a mean stem number connected via adjacent re-entry, $N$, is ∼3. This stem number is well consistent with the experimentally determined $N$ number of 2.5−3 of PLLA in this study.

## 3. DISCUSSION

**3.1. Chain Length in the Adjacent Re-entry Clusters in the Melt-Grown Crystals.** The chain-folding number ($n$ = 1.5−2) of PLLA is independent of $M$ and the experimentally used kinetics ($T_c$ = 90 and 150 °C). As mentioned above, $l$ was determined to be 21.5 and 11.9 nm at $T_c$ = 150 and 90 °C, respectively. Using the $n$ of 1.5 and $l$ values, we roughly estimated a mean value of minimum molecular weight in the adjacent re-entry clusters $M_{ac}$ to be 8.1K and 4.5K g/mol at $T_c$ = 150 and 90 °C, respectively. Note that the fold loop length is not included, and the minimum $n$ value is used in the calculation. Thereby, the real $M_{ac}$ may be longer than the estimated values.

At $T_c$ = 150 °C, crystallization process induces a large $M_{ac}$ of 8.1K g/mol, which is much longer than $M_e$.[63] This comparison implies that reptation mode of the activated chains expel chain entanglement points from the ordered regions to the disordered ones during crystallization. This process leads to spatially heterogeneous distributions of entanglement densities and adjacent re-entry clusters with $n$ of 1.5−2. With decreasing $T_c$, the chain dynamics is lowered. As a result, the $M_{ac}$ value is lowered to 4.5K g/mol. From these simple arguments, it is indicated that reptation mode of polymer chains plays an important role to increase the $M_{ac}$ value as a function of $T_c$. However, even enhanced chain dynamics is insufficient to increase the $n$ value in the melt-grown crystals. Additionally, the $n$ value is independent of $M$. These facts imply that entanglement length changes as a function of $T_c$; however, the presence of entanglements limits the $n$ value in the melt-grown crystals of PLLA with $M \gg M_e$. In a recent MD simulation by Sommer and Luo, it was predicted that entanglement length increases with increasing $T_c$; however, existing entanglements significantly limit adjacent re-entry numbers to ∼1.2 in a wide $T_c$ range.[58,59] Moreover, Hu and Cai proposed intramolecular nucleation mechanism, where nucleation is initiated by a short adjacent re-entry structure.[62] These computational results are well consistent with our experimental results.

**3.2. Intramolecular and Intermolecular Packing in the Solution- and Melt-Grown Crystals.** The melt-grown crystals forms the $\alpha$ crystals above 120 °C and the $\alpha'$ crystals below 100 °C,[10,54,65−69] while the solution-grown crystals form thermodynamically stable $\alpha$ crystals under both slow and rapid crystallizations.[27,28] To understand different packing selections between the melt- and solution-grown crystals as a function of $T_c$, we consider contributions of intermolecular and intramolecular packing structures to the overall ones. The intramolecular packing originates from the adjacent re-entry folding structure. The fact of $T_c$ independence of the $n$ values in both solution- and melt-grown crystals implies that chain-folding process is sufficiently fast and not affected by experimentally used kinetics. Sommer and Luo predicted that the coarse-grained PVA model rapidly folded between entanglements in the melt-grown crystals, and its process is ∼25 ns.[60,61] These computational models are well consistent with the invariant $n$ values obtained in this work. Therefore, it is simply assumed that intramolecular packing process selects the thermodynamically stable $\alpha$ packing structure in both solution and melt-grown crystals even under the rapid quenching conditions. Thereby, increasing the cluster size may be one of the important factors to result in the thermodynamically stable packing structure. In the solution- and melt-grown crystals, there are critical differences between the sizes of the stem clusters via folding (intramolecular cluster). In the former, the nanocluster consists of more than 8 stems, which is much larger than the unit cell size (2 stems per unit cell).[68,69] On the other hand, the latter has 2.5−3 stems, which are comparable to the stem number in the unit cell (Figure 6). Decreasing the cluster size increases contribution of the intermolecular packing to the overall packing structure.

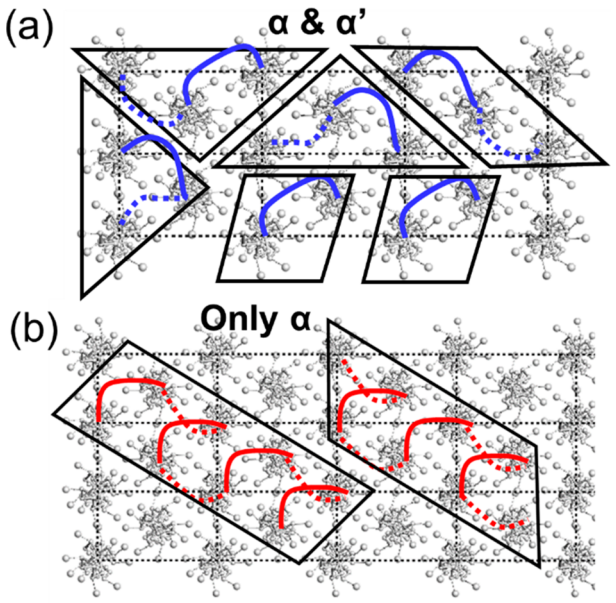


**Figure 6.** Schematic illustrations for the chain-folding structures in (a) the melt- and (b) solution-grown crystals. Intramolecular stem clusters via adjacent re-entry are enclosed by black triangles and parallelograms. Red and blue curves are possible adjacent re-entry patterns.

Under the assumption that the aggregation of the clusters induces intermolecular packing, it might be understood that packing differences between the solution- and melt-grown crystals are related to the dynamics of the clusters and chains. After forming the nanocluster via folding, mobility of the clusters and chains would be significantly affected by presence and absence of entanglements, and temperature. It is considered that there is no entanglement in the dilution solution prior to crystallization. However, it may form some entanglements even in the dilute solution during crystallization process. However, entanglement densities are much higher in the melt state than those in the dilution solution during crystallization. At the high $T_c$s in both solution (90 °C) and melt-grown crystals (150 °C), the mobility of the clusters and chains is sufficiently high to select the thermodynamically stable packing structure even in the condensed melt. In the melt state, the mobility of the chains and clusters is lowered due to entanglements at the low $T_c$. As a result, the limited mobility of the chains and clusters induces higher chances to induce the disordered packing structures in the melt-grown crystals. On the other hand, the less entangled clusters and chains are still possible to select the thermodynami-


DOI: 10.1021/acs.macromol.9b00702
Macromolecules 2019, 52, 4739−4748

cally stable crystals in the solution-grown crystals even under rapid quenching. These are plausible reasons why the melt- and solution-grown crystals choose different packing structures under the large supercooling.

## 4. CONCLUSION

The chain-folding structure, long period, crystallinity, packing structure, and morphology of PLLA samples with three different $M_w$s of 46K−326 K g/mol crystallized at $T_c$ = 150 and 90 °C were studied by various experimental tools. It was found that the chain-folding number ($n$ = 1.5−2) is independent of $M$ and the largely different crystallization kinetics. Combining the $n$ values with the lamellae thickness, the minimum molecular weight in the adjacent re-entry clusters was estimated to be 8.1K and 4.5K g/mol at $T_c$ 150 and 90 °C. These findings indicate that (i) the chain-folding process is a local event in polymer crystallization and (ii) the reptation mode of polymer chains increases $M_{ac}$ at the high $T_c$ but is not sufficient to increase the folding number in the melt-grown crystals. Moreover, different $T_c$ dependences of packing selections between the melt- and solution-grown crystals were explained in terms of effects of intermolecular packing structures due to different entanglement degrees.

## 5. EXPERIMENTAL SECTION

**5.1. Preparation of PLLA Melt-Grown Crystals.** $^{13}$C-labeled PLLA with $M_w$s of 46K ($s$), 90K ($m$), and 326K g/mol ($l$) and nonlabeled PLLA with $M_w$s of 47K, 88K, and 239K g/mol synthesized in our previous works[27,28] were used in this study. The labeled PLLA and nonlabeled PLLA with the weight ratio of 1:9 were dissolved in dichloromethane. Then the solution was cast on the Petri dish. The blended film was obtained after solvent evaporation. PLLA (15 mg) was heated at 200 °C ($T_m$) for 5 min. Then the sample was quickly moved to another hot stage preset at $T_c$ = 90 or 150 °C. The isothermal crystallization time was 8 h.

**5.2. Characterizations.** Polarizing optical microscope observations were performed by using a Nikon ECLIPSE LV100N POL fixed with a sensitive color plate. WAXD experiments were operated on the instrument equipped with a Rigaku Rapid II sealed tube generator and an image plate as the detector. The measuring time for each sample was 15 min. The working voltage and current were 40 kV and 30 mA, respectively. The wavelength of the X-ray was 0.154 nm.

ssNMR experiments were performed on a Bruker AVANCE 300 with a 4 mm double resonance MAS probe at 25 °C. The MAS frequency was set to 5102 ± 5 and 10000 ± 5 Hz. The 90° pulses for $^1$H and $^{13}$C were set as 2.4 and 4.8 $\mu$s, respectively. The recycle delay and CP time were 2 s and 1 ms, respectively. The PostC7[32] sequence with a field strength of 35.7 kHz at the MAS frequency of 5102 Hz was applied to excite and reconvert $^{13}$C−$^{13}$C DQ signals into SQ signals. $^1$H two-pulse phase modulation (TPPM)[81] and continuous wave decoupling with a field strength of 104 kHz were applied to the $^1$H channel during the $^{13}$C acquisition and recoupling periods, respectively. Spin dynamics simulations were calculated by SPINEVOLUTION.[78]

SAXS experiments were performed using the 11-BM beamline, Complex Materials Scattering (CMS) with the X-ray energy of 13.5 keV at the National Synchrotron Light Source II in Upton, NY. The images were captured using a Pilatus 2M area detector. The sample-to-detector distance was 3.03 m. The experiments were conducted at room temperature.

## ■ ASSOCIATED CONTENT

### Supporting Information

The Supporting Information is available free of charge on the ACS Publications website at DOI: 10.1021/acs.macromol.9b00702.

Figures S1−S4 (PDF)

## ■ AUTHOR INFORMATION


### Corresponding Author

*(T.M.) E-mail: miyoshi@uakron.edu.

### ORCID

Wei Chen: 0000-0001-8334-0024
Tadanori Koga: 0000-0003-1316-6133
You-lee Hong: 0000-0001-8568-9828
Toshikazu Miyoshi: 0000-0001-8344-9687


### Notes

The authors declare no competing financial interest.

## ■ ACKNOWLEDGMENTS

This study was financially supported by the National Science Foundation (Grant DMR-178999).

## ■ REFERENCES


(1) Keller, A. A Note on Single Crystals in Polymers: Evidence for a Folded Chain Configuration. *Philos. Mag.* **1957**, *2*, 1171−1175.
(2) Cheng, S. Z. D. *Phase Transitions in Polymers*; Elsevier: 2008.
(3) Lotz, B.; Miyoshi, T.; Cheng, S. Z. D. 50th Anniversary Perspective: Polymer Crystals and Crystallization: Personal Journeys in a Challenging Research Field. *Macromolecules* **2017**, *50*, 5995−6025.
(4) Ungar, G.; Zeng, X. B. Learning Polymer Crystallization with the Aid of Linear, Branched and Cyclic Model Compounds. *Chem. Rev.* **2001**, *101*, 4157−4188.
(5) Strobl, G. From the Melt via Mesomorphic and Granular Crystalline Layers to Lamellar Crystallites: A Major Route Followed in Polymer Crystallization? *Eur. Phys. J. E: Soft Matter Biol. Phys.* **2000**, *3*, 165−183.
(6) Zhu, X.; Yan, D.; Fang, Y. In Situ FTIR Spectroscopic Study of the Conformational Change of Isotactic Polypropylene during the Crystallization Process. *J. Phys. Chem. B* **2001**, *105*, 12461−12463.
(7) Dai, S. P.; Cebe, P.; Capel, M.; Alamo, R. G.; Mandelkern, L. In Situ Wide- and Small-Angle X-ary Scattering Study of Melting Kinetics of Isotactic Polypropylene. *Macromolecules* **2003**, *36*, 4042−4050.
(8) Armistead, J. P.; Hoffman, J. D. Direct Evidence of Regimes I, II, and III in Linear Polyethylene Fractions As Revealed by Spherulite Growth Rates. *Macromolecules* **2002**, *35*, 3895−3913.
(9) Salmerón Sánchez, M.; Mathot, B.F. V.; Vanden Poel, G.; Gómez Ribelles, J. L. Effects of the Cooling Rate aon the Nucleation Kinetics of Poly(L-Lactic Acid) and its Infleunce on Morphology. *Macromolecules* **2007**, *40*, 7989−7997.
(10) Wasanasuk, K.; Tashiro, K. Structural Regularization in the Crystallization Process from the Glass or Melt of Poly(l-Lactic Acid) Viewed from the Temperature-Dependent and Time-Resolved Measurements of FTIR and Wide-Angle/Small-Angle X-Ray Scatterings. *Macromolecules* **2011**, *44*, 9650−9660.
(11) Ono, Y.; Kumaki, J. In Situ Real-Time Observation of Polymer Folded-Chain Crystallization by Atomic Force Microscopy at the Molecular Level. *Macromolecules* **2018**, *51*, 7629−7636.
(12) Savage, R. C.; Mullin, N.; Hobbs, J. K. Molecular Conformation at the Crystal-Amorphous Interface in Polyethylene. *Macromolecules* **2015**, *48*, 6160−6165.
(13) Stehling, F. C.; Ergos, E.; Mandelkern, L. Phase Separation in N-Hexatriacontane-n-Hexatriacontane-d 74 and Polyethylene-Poly-(Ethylene-d 4) Systems. *Macromolecules* **1971**, *4*, 672−677.
(14) Sadler, D. M.; Keller, A. Neutron Scattering of Solution-Grown Polymer Crystals: Molecular Dimensions Are Insensitive to Molecular Weight. *Science* **1979**, *203*, 263−265.
(15) Sadler, D. M.; Harris, R. A Neutron Scattering Analysis: How Does the Conformation in Polyethylene Crystals Reflect That in the Melt? *J. Polym. Sci., Polym. Phys. Ed.* **1982**, *20*, 561−578.
(16) Guttman, C. M.; DiMarzio, E. A.; Hoffman, J. D. Calculation of SANS Intensity for Polyethylene: Effect of Varying Fold Planes and Fold Plane Roughening. *Polymer* **1981**, *22*, 597−608.




DOI: 10.1021/acs.macromol.9b00702
*Macromolecules* 2019, 52, 4739−4748

(17) Spells, S. J.; Sadler, D. M.; Keller, A. Chain Trajectory in Solution Grown Polyethylene Crystals: Correlation between Infra-Red Spectroscopy and Small-Angle Neutron Scattering. *Polymer* **1980**, *21*, 1121−1128.
(18) Jing, X.; Krimm, S. Mixed-Crystal Infrared Studies of Chain Folding in Melt-Crystallized Polyethylene. *J. Polym. Sci., Polym. Lett. Ed.* **1983**, *21*, 123−130.
(19) Jing, X.; Krimm, S. Mixed-Crystal Infrared Studies of Chain Folding in Polyethylene Single Crystals: Effect of Crystallization Temperature. *J. Polym. Sci., Polym. Phys. Ed.* **1982**, *20*, 1155−1173.
(20) Zeng, X.; Ungar, G.; Spells, S. J.; King, S. M. Real-Time Neutron Scattering Study of Transient Phases in Polymer Crystallization. *Macromolecules* **2005**, *38*, 7201−7204.
(21) Hong, Y. L.; Miyoshi, T. Chain-Folding Structure of a Semicrystalline Polymer in Bulk Crystals Determined by C-13-C-13 Double Quantum NMR. *ACS Macro Lett.* **2013**, *2*, 501−505.
(22) Hong, Y. L.; Miyoshi, T. Elucidation of the Chain-Folding Structure of a Semicrystalline Polymer in Single Crystals by Solid-State NMR. *ACS Macro Lett.* **2014**, *3*, 556−559.
(23) Hong, Y. L.; Yuan, S.; Li, Z.; Ke, Y.; Nozaki, K.; Miyoshi, T. Three-Dimensional Conformation of Folded Polymers in Single Crystals. *Phys. Rev. Lett.* **2015**, *115*, 1−5.
(24) Hong, Y. L.; Chen, W.; Yuan, S.; Kang, J.; Miyoshi, T. Chain Trajectory of Semicrystalline Polymers As Revealed by Solid-State NMR Spectroscopy. *ACS Macro Lett.* **2016**, *5*, 355−358.
(25) Hong, Y. L.; Koga, T.; Miyoshi, T. Chain Trajectory and Crystallization Mechanism of a Semicrystalline Polymer in Melt- and Solution-Grown Crystals As Studied Using $^{13}$C- $^{13}$C Double-Quantum NMR. *Macromolecules* **2015**, *48*, 3282−3293.
(26) Li, Z.; Hong, Y. L.; Yuan, S.; Kang, J.; Kamimura, A.; Otsubo, A.; Miyoshi, T. Determination of Chain-Folding Structure of Isotactic Polypropylene in Melt-Grown $\alpha$ Crystals by $^{13}$C- $^{13}$C Double Quantum NMR and Selective Isotopic Labeling. *Macromolecules* **2015**, *48*, 5752−5760.
(27) Wang, S.; Yuan, S.; Chen, W.; He, Q.; Hong, Y. L.; Miyoshi, T. Solid-State NMR Study of the Chain Trajectory and Crystallization Mechanism of Poly(l-Lactic Acid) in Dilute Solution. *Macromolecules* **2017**, *50*, 6404−6414.
(28) Wang, S.; Yuan, S.; Chen, W.; Zhou, Y.; Hong, Y. L.; Miyoshi, T. Structural Unit of Polymer Crystallization in Dilute Solution As Studied by Solid-State NMR and $^{13}$C Isotope Labeling. *Macromolecules* **2018**, *51*, 8729−8737.
(29) Yuan, S.; Li, Z.; Hong, Y. L.; Ke, Y.; Kang, J.; Kamimura, A.; Otsubo, A.; Miyoshi, T. Folding of Polymer Chains in the Early Stage of Crystallization. *ACS Macro Lett.* **2015**, *4*, 1382−1385.
(30) Yuan, S.; Li, Z.; Kang, J.; Hong, Y. L.; Kamimura, A.; Otsubo, A.; Miyoshi, T. Determination of Local Packing Structure of Mesomorphic Form of Isotactic Polypropylene by Solid-State NMR. *ACS Macro Lett.* **2015**, *4*, 143−146.
(31) Wang, S.; Hong, Y. L.; Yuan, S.; Chen, W.; Zhou, W.; Li, Z.; Wang, K.; Min, X.; Konishi, T.; Miyoshi, T. Chain Trajectory, Chain Packing, and Molecular Dynamics of Semicrystalline Polymers as Studied by Solid-State NMR. *Polymers (Basel, Switz.)* **2018**, *10*, 775.
(32) Hohwy, M.; Jakobsen, H. J.; Edén, M.; Levitt, M. H.; Nielsen, N. C. Broadband Dipolar Recoupling in the Nuclear Magnetic Resonance of Rotating Solids: A Compensated C7 Pulse Sequence. *J. Chem. Phys.* **1998**, *108*, 2686−2694.
(33) Tanzawa, Y. Growth rate and morphology of isotactic polystyrene crystals in solution at high supercoolings. *Polymer* **1992**, *33*, 2659−2665.
(34) Wunderlich, B.; James, E. A.; Shu, T. Crystallization of Polyethylene from O-Xylene. *J. Polym. Sci., Part A: Gen. Pap.* **1964**, *2*, 2759−2769.
(35) Xu, H.; Matkar, R.; Kyu, T. Phase-Field Modeling on Morphological Landscape of Isotactic Polystyrene Single Crystals. *Phys. Rev. E* **2005**, *72*, 011804.
(36) Zhang, J.; Muthukumar, M. Monte Carlo Simulations of Single Crystals from Polymer Solutions. *J. Chem. Phys.* **2007**, *126*, 234904.
(37) Point, J. J.; Villers, D. Nucleation-Controlled Growth and Normal Growth: A Unified View. *J. Cryst. Growth* **1991**, *114*, 228−238.
(38) Toda, A. Rounded Lateral Habits of Polyethylene Single Crystals. *Polymer* **1991**, *32*, 771−780.
(39) Putra, E. G. R.; Ungar, G. Step Initiation and Propagation Rate Minimum in Solution Crystallization of Five Long Alkanes. *Macromolecules* **2003**, *36*, 3812−3814.
(40) Shcherbina, M. A.; Ungar, G. Asymmetric Curvature of Growth Faces of Polymer Crystals. *Macromolecules* **2007**, *40*, 402−405.
(41) Allegra, G.; Meille, S. V. Pre-Crystalline, High-Entropy Aggregates: A Role in Polymer Crystallization? *Adv. Polym. Sci.* **2005**, *191*, 87−135.
(42) Allegra, G.; Famulari, A. Chain Statistics in Polyethylene Crystallization. *Polymer* **2009**, *50*, 1819−1829.
(43) Welch, P.; Muthukumar, M. Molecular Mechanisms of Polymer Crystallization from Solution. *Phys. Rev. Lett.* **2001**, *87*, 218302.
(44) Liu, C.; Muthukumar, M. Langevin Dynamics Simulations of Early-Stage Polymer Nucleation and Crystallization. *J. Chem. Phys.* **1998**, *109*, 2536−2542.
(45) Fujiwara, S.; Sato, T. Molecular Dynamics Simulations of Structural Formation of a Single Polymer Chain: Bond-Orientational Order and Conformational Defects. *J. Chem. Phys.* **1997**, *107*, 613.
(46) Hoffman, J. D.; Miller, R. L. Kinetic of Crystallization from the Melt and Chain Folding in Polyethylene Fractions Revisited: Theory and Experiment. *Polymer* **1997**, *38*, 3151−3212.
(47) Dealy, J. M.; Larson, R. G. *Structure and Rheology of Molten Polymers*; Carl Hanser Verlag GmbH & Co. KG: München, 2006.
(48) Ungar, G.; Stejny, J.; Keller, A.; Bidd, I.; Whiting, M. C. The Crystallization of Ultralong Normal Paraffins: The Onset of Chain Folding. *Science* **1985**, *229*, 386−389.
(49) Ungar, G.; Keller, A. Time-Resolved Synchrotron X-Ray Study of Chain-Folded Crystallization of Long Paraffins. *Polymer* **1986**, *27*, 1835−1844.
(50) Ungar, G.; Zeng, X. B.; Spells, S. J. Non-Integer and Mixed Integer Forms in Long n-Alkanes Observed by Real-Time LAM Spectroscopy and SAXS. *Polymer* **2000**, *41*, 8775−8780.
(51) Song, K.; Krimm, S. Mixed-Integer and Fractional-Integer Chain Folding in Crystalline Lamellae of Poly(Ethylene Oxide): A Raman Longitudinal Acoustic Mode Study. *Macromolecules* **1989**, *22*, 1504−1505.
(52) Song, K.; Krimm, S. Raman Longitudinal Acoustic Mode (LAM) Studies of Folded-Chain Morphology in Poly(Ethylene Oxide) (PEO). 3. Chain Folding in PEO as a Function of Molecular Weight. *Macromolecules* **1990**, *23*, 1946−1957.
(53) Yamashita, M. Regime II-III Transition in Isotactic Polybutene-1 Tetragonal Crystal Growth. *Polymer* **2014**, *55*, 733−737.
(54) Kawai, T.; Rahman, N.; Matsuba, G.; Nishida, K.; Kanaya, T.; Nakano, M.; Okamoto, H.; Kawada, J.; Usuki, A.; Honma, N.; et al. Crystallization and Melting Behavior of Poly (L-Lactic Acid). *Macromolecules* **2007**, *40*, 9463−9469.
(55) Cho, T. Y.; Strobl, G. Temperature Dependent Variations in the Lamellar Structure of Poly(l-Lactide). *Polymer* **2006**, *47*, 1036−1043.
(56) Abe, H.; Kikkawa, Y.; Inoue, Y.; Doi, Y. Morphological and Kinetic Analyses of Regime Transition of Poly[(S)-Lactide] Crystal Growth. *Biomacromolecules* **2001**, *2*, 1007−1014.
(57) Di Lorenzo, M. L. Crystallization Behavior of Poly(l-Lactic Acid). *Eur. Polym. J.* **2005**, *41*, 569−575.
(58) Luo, C.; Kröger, M.; Sommer, J. U. Entanglements and Crystallization of Concentrated Polymer Solutions: Molecular Dynamics Simulations. *Macromolecules* **2016**, *49*, 9017−9025.
(59) Luo, C.; Sommer, J. U. Role of Thermal History and Entanglement Related Thickness Selection in Polymer Crystallization. *ACS Macro Lett.* **2016**, *5*, 30−34.
(60) Luo, C.; Sommer, J. U. Frozen Topology: Entanglements Control Nucleation and Crystallization in Polymers. *Phys. Rev. Lett.* **2014**, *112*, 1−5.
(61) Luo, C.; Sommer, J. U. Growth Pathway and Precursor States in Single Lamellar Crystallization: MD Simulations. *Macromolecules* **2011**, *44*, 1523−1529.


DOI: 10.1021/acs.macromol.9b00702
*Macromolecules* 2019, 52, 4739−4748

(62) Hu, W.; Cai, T. Regime Transitions of Polymer Crystal Growth Rates: Molecular Simulations and Interpretation beyond Lauritzen-Hoffman Model. *Macromolecules* **2008**, *41*, 2049−2061.
(63) Razavi, M.; Wang, S. Q. Why fully crystalline poly(Lactic Acid) is britle at room temperature? Submitted to *Macromolecules*.
(64) Zhang, J.; Duan, Y.; Sato, H.; Tsuji, H.; Noda, I.; Yan, S.; Ozaki, Y. Crystal Modifications and Thermal Behavior of Poly (L -Lactic Acid) Revealed by Infrared Spectroscopy. *Macromolecules* **2005**, *38*, 8012−8021.
(65) Pan, P.; Zhu, B.; Kai, W.; Dong, T.; Inoue, Y. Effect of Crystallization Temperature on Crystal Modifications and Crystallization Kinetics of Poly(L-Lactide). *J. Appl. Polym. Sci.* **2008**, *107*, 54−62.
(66) Pan, P.; Yang, J.; Shan, G.; Bao, Y.; Weng, Z.; Cao, A.; Yazawa, K.; Inoue, Y. Temperature-Variable FTIR and Solid-State $^{13}$C NMR Investigations on Crystalline Structure and Molecular Dynamics of Polymorphic Poly(l -Lactide) and Poly(l -Lactide)/Poly(d -Lactide) Stereocomplex. *Macromolecules* **2012**, *45*, 189−197.
(67) Lotz, B. Crystal Polymorphism and Morphology of Polylactides. *Synthesis, Structure and Properties of Poly(lactic acid)*; Springer: Cham, 2017; pp 273−302.
(68) Sasaki, S.; Asakura, T. Helix Distortion and Crystal Structure of the $\alpha$ -Form of Poly (L -Lactide). *Macromolecules* **2003**, *36*, 8385−8390.
(69) Wasanasuk, K.; Tashiro, K. Crystal Structure and Disorder in Poly(l-Lactic Acid) $\delta$ Form ($\alpha$' Form) and the Phase Transition Mechanism to the Ordered $\alpha$ Form. *Polymer* **2011**, *52*, 6097−6109.
(70) Thakur, K. A. M.; Kean, R. T.; Zupfer, J. M.; Buehler, N. U.; Doscotch, M. A.; Munson, E. J. Solid State $^{13}$C CP-MAS NMR Studies of the Crystallinity and Morphology of Poly (L -Lactide). *Macromolecules* **1996**, *29*, 8844−8851.
(71) Chen, W.; Reichert, D.; Miyoshi, T. Short-Range Correlation of Successive Helical Jump Motions of Poly(L-Lactic Acid) Chains in the $\alpha$ Phase as Revealed by Solid-State NMR. *J. Phys. Chem. B* **2015**, *119*, 4552−4563.
(72) Chen, W.; Zhou, W.; Makita, Y.; Wang, S.; Yuan, S.; Konishi, T.; Miyoshi, T. Characterization of the Slow Molecular Dynamics of Poly(l-Lactic Acid) in $\alpha$ and $\alpha$' Phases, in a Glassy State, and in a Complex with Poly(d-Lactic Acid) by Solid-State NMR. *Macromol. Chem. Phys.* **2018**, *219*, 1700451.
(73) Yang, X.; Kang, S.; Yang, Y.; Aou, K.; Hsu, S. L. Raman Spectroscopic Study of Conformational Changes in the Amorphous Phase of Poly(Lactic Acid) during Deformation. *Polymer* **2004**, *45*, 4241−4248.
(74) Yang, X.; Kang, S.; Hsu, S. L.; Stidham, H. D.; Smith, P. B.; Leugers, A. A Spectroscopic Analysis of Chain Flexibility of Poly(Lactic Acid). *Macromolecules* **2001**, *34*, 5037−5041.
(75) Garlotta, D. A Literature Review of Poly (Lactic Acid). *J. Polym. Environ.* **2001**, *9*, 63−84.
(76) Lotz, B. Single Crystals of the Frustrated $\beta$-Phase and Genesis of the Disordered $\alpha$'-Phase of Poly(l -Lactic Acid). *ACS Macro Lett.* **2015**, *4*, 602−605.
(77) Levitt, M. *Spin Dynamics: Basics of Nuclear Magnetic Resonance*; John Wiley and Sons: 2000.
(78) Veshtort, M.; Griffin, R. G. SPINEVOLUTION: A Powerful Tool for the Simulation of Solid and Liquid State NMR Experiments. *J. Magn. Reson.* **2006**, *178*, 248−282.
(79) Hoffman, J. D. Regime III Crystallization in Melt-Crystallized Polymers: The Variable Cluster Model of Chain Folding. *Polymer* **1983**, *24*, 3−26.
(80) Kaihara, S.; Matsumura, S.; Mikos, A. G.; Fisher, J. P. Synthesis of Poly(L-Lactide) and Polyglycolide by Ring-Opening Polymerization. *Nat. Protoc.* **2007**, *2*, 2767−2771.
(81) Bennett, A. E.; Rienstra, C. M.; Auger, M.; Lakshmi, K. V.; Griffin, R. G. Heteronuclear Decoupling in Rotating Solids. *J. Chem. Phys.* **1995**, *103*, 6951.



DOI: 10.1021/acs.macromol.9b00702
*Macromolecules* 2019, 52, 4739−4748